Regular Article

# Multi-scale undulations in human aortic endothelial cell fibers

Jolie B. Frketic[1], Abigail DeLaPeña[2], Melanie G. Suaris[3], Steven M. Zehnder[2], and Thomas E. Angelini[2,3,4,a]

[1] Department of Industrial and Manufacturing Engineering, Florida State University, Tallahassee, FL, 32310, USA
[2] Department of Mechanical and Aerospace Engineering, University of Florida, Gainesville, FL, 32611, USA
[3] J. Crayton Pruitt Family Department of Biomedical Engineering, University of Florida, Gainesville, FL, 32611, USA
[4] Institute for Cell Engineering and Regenerative Medicine, University of Florida, Gainesville, FL, 32611, USA

**Abstract.** Blood vessels often have an undulatory morphology, with excessive bending, kinking, and coiling occuring in diseased vasculature. The underlying physical causes of these morphologies are generally attributed, in combination, to changes in blood pressure, blood flow rate, and cell proliferation or apoptosis. However, pathological vascular morphologies often start during developmental vasculogenesis. At early stages of vasculogenesis, angioblasts (vascular endothelial cells that have not formed a lumen) assemble into primitive vessel-like fibers before blood flow occurs. If loose, fibrous aggregates of endothelial cells can generate multi-cellular undulations through mechanical instabilities, driven by the cytoskeleton, new insight into vasculature morphology may be achieved with simple *in vitro* models of endothelial cell fibers. Here we study mechanical instabilities in vessel-like structures made from endothelial cells embedded in a collagen matrix. We find that endothelial cell fibers contract radially over time, and undulate at two dominant wavelengths: approximately 1 cm and 1 mm. Simple mechanical models suggest that the long-wavelength undulation is Euler buckling in rigid confinement, while the short-wavelength buckle may arise from a mismatch between fiber bending energy and matrix deformation. These results suggest a combination of fiber-like geometry, cystoskeletal contractions, and extracellular matrix elasticity may contribute to undulatory blood vessel morphology in the absence of a lumen or blood pressure.

## 1 Introduction

Cells within most types of tissue sense the stiffness of their surroundings by exerting forces on the extracellular matrix (ECM) and on one another [1–3]. Cells sense stiffness and forces through processes of mechanotransduction, in which mechanical strains on membrane-associated protein complexes lead to a cascade of signals within the cell, feeding back to modulate cell mechanical behaviors. In blood vessels, this cascade of mechanotransduction-associated biochemical signals can occur in response to changes in blood pressure and flow rate; endothelial cells at the lumen-blood interface sense changes in shear stress when blood flow rate changes, and both smooth muscle cells and endothelial cells sense stretching when blood vessels are forced to dilate under increased blood pressure [4]. In both mature and growing vessels, the normal physiological response to these physical cues is a change in wall thickness or vessel diameter [5–7]. However, pathological conditions of blood vessels generate other types of morphological change, including increased tortuosity, kinking and coiling [8–10]. The physical origin of these morphologies may be mechanical buckling, arising from force imbalances associated with cell proliferation and apoptosis or changes in ECM stiffness. Physical models of this buckling show that the forces associated with blood pressure may not play a major role [11]. These pathological morphologies —bending, kinking, and coiling— are found in mature arteries, but may start during embryonic development [12]. Interestingly, at the earliest stages of vasculogenesis in embryos, before lumen formation, angioblast aggregation into vessel-like structures are not likely to involve the support of fluid pressure [13,14]. Mechanical instabilities within primitive vessel-like structures have not been explored. Investigation of mechanical instabilities that arise in these vessel-like structures, in the absence of a developed lumen or blood pressure, may provide new insights into blood vessel morphology.

Here we study mechanical instabilities endothelial cell fibers —molded cylinders of collagen-ECM permeated with endothelial cells— confined in agar tubes. These fibers are much larger and simpler than the fine, complex, endothelial cell plexus that emerges during development, and provide a starting point for understanding multi-cellular mechanics in high-aspect ratio structures. Cell fibers are imaged with two-photon fluorescence microscopy, time-lapse bright-field microscopy, time-lapse macro-imaging, and time-lapse small-angle
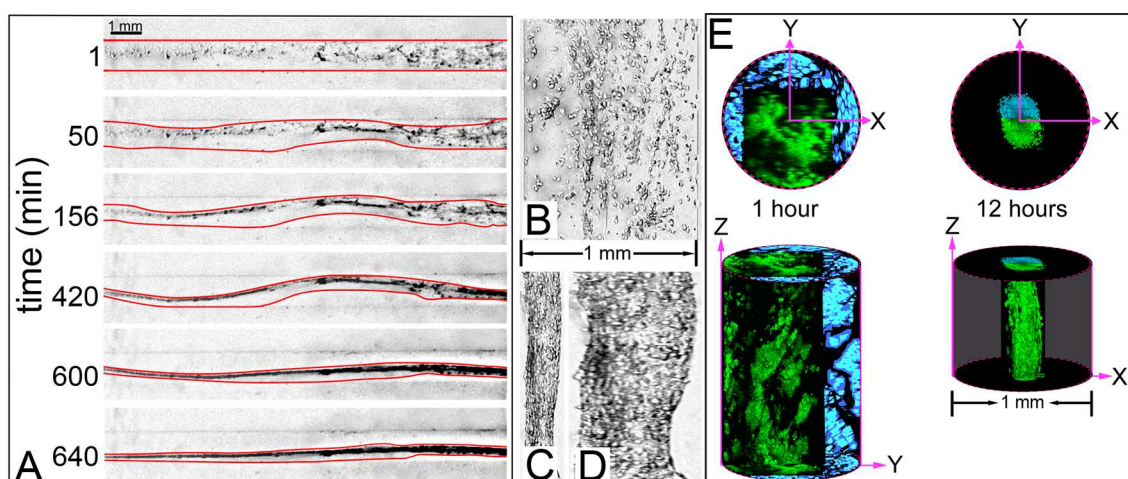
a e-mail: t.e.angelini@ufl.edu

**Fig. 1.** Time-lapse photographs of endothelial cell fibers show a radial collapse and lateral undulations over time. Photographs are taken with back-lighting, and are inherently low contrast. Photos are shown at saturated contrast with hand-drawn outlines to aid the reader (A). Time-lapse microscopy shows a sparsely populated cell fiber before the collapse (B) and a densely populated cell fiber after the collapse, at $t = 17$ hours after seeding the cells (C, same scale as B). By digitally stretching the micrograph in (C) by a factor of five, a short-wavelength undulation of fiber shape is seen (D). Maximum intensity projections of stacks collected with two-photon confocal microscopy shows cells dispersed throughout the cylinder in interconnected clusters for cells fixed and stained one hour after seeding. Twelve hours after seeding, the fiber has collapsed and appears to have lower cell density near the center of the fiber. Green sections are imaged volumes; blue sections are hypothesized illustrations of the cell distribution outside the field of view, based on our other observations.

light scattering (SALS). We find that the endothelial cells contract the entire fiber over time, pulling the collagen-cell matrix inward, away from the walls of the tubular support. As the fiber collapses, cells accumulate at the fiber's outer periphery, and buckling of the linear structure occurs. Microscopy, macro-imaging, and SALS reveal a multi-scale bucking phenomenon. At the macro-scale, of order $\sim 1\,\mathrm{cm}$, we observe a long-wavelength bend of the fiber, and at the scale of about $1\,\mathrm{mm}$, a second small-wavelength undulation occurs. Mechanical models suggest that the long-wavelength undulation is Euler buckling in rigid confinement. By considering the potential role of elastic-support provided by the collagen ECM, we predict a short-wavelength buckle that agrees very well with data collected using all imaging and scattering methods. These results suggest that undulatory blood vessel morphology can be established in the absence of a lumen or blood pressure, given a fiber-like geometry and sufficient levels of cytoskeletal contraction forces.

## 2 Results

To investigate potential mechanical instabilities in endothelial cell fibers, approximately $10^5$ human aortic endothelial cells (HAECs) are dispersed in cell growth medium mixed with type-I collagen, and pipetted into a $1\,\mathrm{mm}$ diameter, $30\,\mathrm{mm}$ length, cylindrical pore before the collagen polymerizes. The cylindrical pore is made by casting a mixture of low-melting temperature agar and cell growth medium around a $1\,\mathrm{mm}$ diameter micropipette, which is removed after the agar-media mixture solidifies.

The solidified agar-media material is brought to $37\,^{\circ}\mathrm{C}$ and neutral $p$H in an incubator before pipetting the cell-collagen mixture into the cylindrical pore. The agar-media mixture generates a large volume of solid growth media that provides sufficient nutrients to feed the cells for several days.

We characterize the fiber morphology and cell distribution in several ways. time-lapse macro-photography, performed in an incubation chamber, shows that the fiber collapses radially and undulates in the transverse direction over the course of about ten hours after seeding the cells. The same process is observed under bright-field microscopy. The small field of view under the microscope precludes observation of the long-wavelength undulation, but reveals the development of a shorter wavelength shape change. This short-wavelength undulation is made clear by stretching the digital image in the radial direction (fig. 1A-D). The cell-driven collapse of collagen matrices seeded with cells is a well-known phenomenon, though the related mechanical instabilities of cell-generated tension in high aspect ratio assemblies like fibers has not been explored [15].

To visualize the spatial cell distribution, two-photon fluorescence microscopy is performed on cell fibers in which the cells are dyed with 5-chloromethylfluorescein diacetate (CMFDA). At early times, cells appear to be distributed throughout the fiber in inter-connected clusters and at later times, cells are evenly packed, but appear to have a lower number density at the center of the fiber than at the edge of the fiber, suggesting that some cells move toward the edge of the fiber as it collapses (fig. 1E).

## 2.1 Multi-scale shape undulations

To characterize fiber shape quantitatively over time, macro-photography and microscopy time-lapse data are investigated using Fourier mode analysis [16–18]. The fiber surface is difficult to detect in macro-photography, imaged at a magnification of $5.5\,\mu$m/pixel, so images are band-passed filtered to smooth out micro-scale details smaller than about $100\,\mu$m. In the filtered images, the backbone of the fiber appears as a dark band of intensity. The backbone $X$-$Y$ coordinates are found by fitting a Gaussian peak to the intensity profile along the horizontal axis at each location along the vertical axis. These coordinates are mapped into $\theta$-$s$ space, where $\theta$ is the tangential angle at location $s$ along the contour of the fiber. A power spectrum of the tangent angle is computed with a discrete cosine transform (DCT), given by $S(q) = |\text{DCT}[\theta(s)]|^2$. A strong peak is observed in $S(q)$ at low $q$, corresponding to length scales of $\lambda_L \sim 10$–$20\,$mm, arising from the long-wavelength undulation directly observed in the images. Surprisingly, a second peak is observed in $S(q)$ at higher $q$'s, corresponding to shorter wavelengths on the order of $\lambda_S \sim 1\,$mm (fig. 2A-C). When cells are intentionally killed at the end of experiments by cutting off the $CO_2$ supply, we observe that the fibers straighten out again, highlighting the role of living cell activity in fiber undulation (fig. 2D). To test the role of cytoskeletal contraction in generating fiber undulation, cells are treated with Blebbistatin, a Myosin II inhibitor. In cells treated with a moderate level ($20\,\mu$M) of Blebbistatin, the amplitude of undulation decreases by over an order of magnitude (fig. 2E).

Shape fluctuations associated with the much weaker peak at high-$q$ are difficult to directly observe in macro-photographs, so a similar Fourier analysis is performed on images collected with microscopy in an environmentally controlled incubation chamber, maintained at $37\,^\circ$C and $5\%$ $CO_2$. The sample is oriented with the long axis of the fiber laying perpendicular to the optical axis, and $Z$-stacks are collected spanning the entire fiber cross-section. Stacks are processed with a stack-focusing algorithm in ImageJ, producing a high-contrast intensity map with sharp boundaries at the fiber surface. The $X$-$Y$ coordinates of the fiber boundaries are identified in a similar manner as with the fiber center, described above, and Fourier shape analysis is performed. The resulting power spectrum of fiber edge shape from microscopy exhibits a single peak at wavelengths of $\lambda_{ms} \sim 1\,$mm, approximately the same as $\lambda_S$ observed in macro-photography (fig. 2D,E). This millimeter-scale undulation can be directly seen in the micrographs shown in fig. 1.

## 2.2 Radial cell distribution

We explore potential changes in cell distribution along the radial direction as the fiber collapses and undulates using both time-lapse microscopy and small-angle light scattering (SALS). Slices from $Z$-stacks collected over time
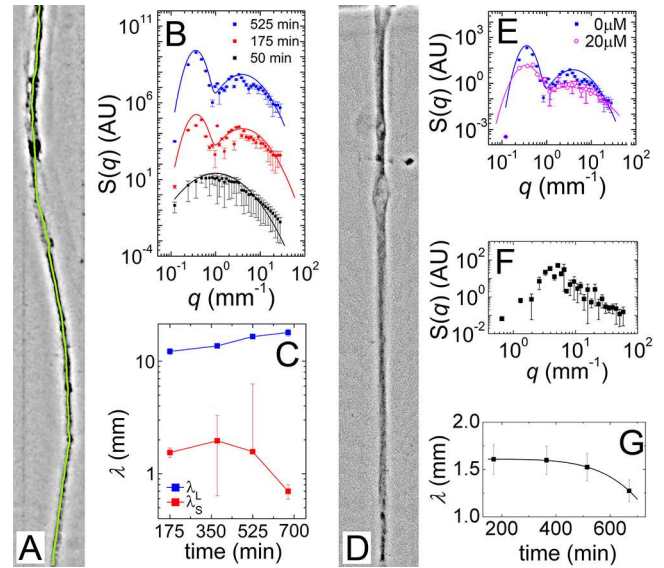


**Fig. 2.** By fitting a Gaussian intensity profile across all 550 horizontal slices along the length of the fiber image, we determine the backbone coordinates of the fiber. A sample backbone profile overlaid onto a contrast-saturated image of the fiber is shown (A). The $X$-$Y$ backbone coordinates are converted into $\theta$-$s$ space, where $\theta$ is the local tangent angle at location $s$ along the length of the backbone. The power spectrum of $\theta$ reveals two strong modes: one with a wavelength of $\lambda_L \sim 10$–$20\,$mm, and another with a wavelength of $\lambda_S \sim 0.7$–$2\,$mm. (B,C) The broad peaks in $S(q)$ are fit with log-normal curves to determine peak positions (B), where errorbars in (C) are $95\%$ confidence intervals of the fitted peak positions. When cells are intentionally killed at the end of experiments, the fiber straightens out again (D), and cells treated with $20\,\mu$M Blebbistatin generate undulations more than an order of magnitude smaller than undrugged cells (E). The same analysis is performed on the surface contours of micrographs (F) revealing a strong short-wavelength undulation, $\lambda_{ms} \sim 1$–$2\,$mm (G).

with bright-field microscopy, as described above, are averaged along the $Z$-direction to generate an approximate 2D map of light absorption through the fiber. This absorption map is averaged along the fiber axis, producing a 1D map of absorption across the fiber, described by Beer's law, $I(r)/I_0 = e^{-h(r)/k(r)}$, where $h(r)$ is the optical path length over which light absorption occurs, $k(r)$ is a spatially varying decay constant, $I_0$ is the incident light intensity, and $-\log[I(r)/I_0]$ is the absorbance. We find that the absorbance is low and noisy across the fiber at early times, when cells are distributed throughout the fiber. As the fiber begins to collapse, the absorbance profile narrows in width and develops a strong minimum at the center of the fiber. This trend continues until the fiber diameter reaches a minimum and the central dip in absorbance is maximized relative to the edges of the fiber.

To test whether these absorption maps could be produced by cylindrical cell distributions, we compute model absorbance maps using Beer's law, assuming that $h(r)$ is the projected length across a circle while varying $k(r)$ in a binary manner, representing regions of high cell density
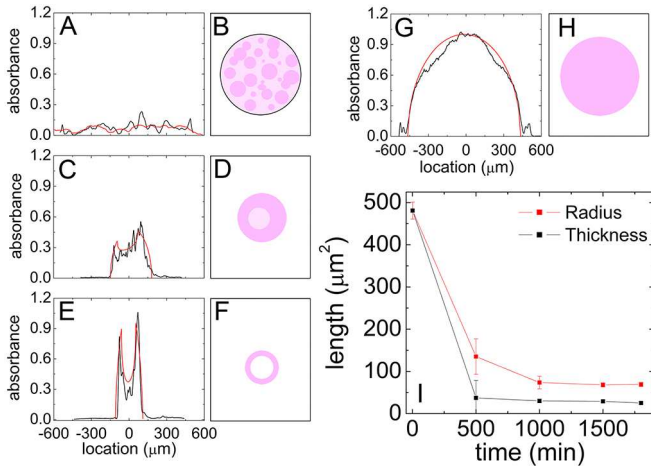
**Fig. 3.** We measure light absorbance across the collapsing fiber using bright-field microscopy. At early times, the average absorbance profile along the width of the fiber is weak, flat, and noisy (A, black line). This absorbance profile can be modeled by assuming a polydisperse distribution of strongly absorbing clusters spread throughout a weakly absorbing circular cross section (B, red line in A). After 500 minutes, the absorbance profile exhibits two peaks near the edge of the fiber and a dip near the fiber center (C, black line), which is consistent with the absorbance profile across a core-shell distribution of high density in the outer regions and low density near the center of the fiber (D, C red line). At 1500 minutes, the absorbance peaks have moved further inward, sharpened, and grown relative to the central dip (E). This profile is also well modeled by a core-shell distribution (E, F red line). This method, when applied to a homogeneously absorbing cylinder filled with diffusing microspheres, produces the expected parabolic profile arising from projecting an absorbing circular cross section onto a single axis (G, H, black line is data, red line is fit). We extract an approximate radius and thickness of the fiber over time by identifying the halfway point of the strong rising edges and dropping central dips, using the width of the rise or drop as an experimental uncertainty (I).

and low cell density. At early times, before the fiber collapses, $k(r)$ is modelled as a polydisperse distribution of clusters. At late times, $k(r)$ is modelled with a step function, corresponding to a cylindrical tube. These minimal models of cell distribution capture the experimental absorption maps very well, and this method is tested by conducting experiments in which the agar pores are filled with $1\,\mu m$ microspheres that diffuse and spread homogenously throughout the cylinders. The profile is parabolic, as expected from projecting a homogeneously absorbing circle onto a single axis. These results suggest that cells spontaneously accumulate with higher density near the periphery of the cell fiber than near the fiber center (fig. 3).

To explore the cell distribution within fibers with a second approach, we perform SALS measurements on samples prepared in $\sim 5\,mm$ thick chambers with optical-grade quartz entrance and exit windows. The SALS instrument is constructed to replicate systems used in measuring dense colloidal materials, with an incident beam that is spread and collimated to a diameter of 1 cm, covering

a very large sample spot [19]. SALS is performed in time lapse, so samples are measured in an incubation chamber maintained at $37\,°C$ and $5\%$ $CO_2$. To minimize multiple scattering and light absorption, a near-infrared diode laser is used, having a wavelength of $830\,nm$ and an output power of $12\,mW$. Although very low laser power levels are used, and the laser is spread over a diameter of about 1 cm, a shuttering system is synched with the digital camera to minimize cell exposure to laser light throughout $\sim 1200$ minute experiments.

The scattering patterns exhibit a strong horizontal band of fringes along the equatorial direction, $q_r$, at $q_z = 0$, characteristic of scattering from cylindrical objects. The initial fringe spacing corresponds perfectly to the dimensions of the cylindrical agar tube that supports the endothelial cell fiber. At later times, a second intensity modulation emerges, corresponding to the smaller diameter of the collapsing cell fiber. To extract the distribution of cells along the radial direction, we model the spatial variation of dielectric constant as a series of twenty cylindrical shells in cylindrical coordinates, each with individual uniform dielectric constant, $\varepsilon_j$, and with fixed edges distributed evenly from $r = 0$ to $r = 500\,\mu m$. The supporting agar tube is modeled as a step function along the $r$-direction. The Fourier transform of this distribution can be computed analytically in cylindrical coordinates, and is given by

$$\tilde{\varepsilon}(q) = \sum_{j=1}^{N-1} \varepsilon_j q^{-1} \left( r_j J_1(qr_j) - r_{j+1} J_1(qr_{j+1}) \right) - \Delta\varepsilon q^{-1} J_1(qr_N),$$

where $J_1$ is the first order Bessel function, $r_j$ and $r_{j+1}$ are the edges of each shell, $r_N$ is the radius of the agar tube, and $\Delta\varepsilon$ is the dielectric contrast between liquid cell growth media and agar. The measured intensity distribution is given by $S(q_r) = |\tilde{\varepsilon}(q_r)|^2$. To achieve good fits an incoherent background term proportional to $q_r^{-2}$ is added, which may arise from scattering through the agar network far from the cell fiber.

With this formulation of the scattering model, there are 22 fitting parameters. To reduce the number of fitting parameters, each $\varepsilon_j$ is constrained to a skewed Gaussian profile, which can describe a wide range of cell distributions. The skewed Gaussian curve used is

$$\varepsilon(r) = A \left( 1 + \mathrm{erf}\left( \alpha \frac{r-\mu}{\sqrt{2\sigma^2}} \right) \right) e^{-\frac{(r-\mu)^2}{2\sigma^2}},$$

where $A$ is an overall amplitude, $\mu$ is the peak location of the Gaussian, $\sigma$ is the width of the Gaussian, and $\alpha$ modulates the degree of skewness independent of $\sigma$. This approach reduces the total number of fitting parameters from 22 to 5, facilitating the efficient execution of nonlinear least-squares fitting (fig. 4A-B).

The fits of $\varepsilon(r)$ are broad at early times, with a weak peak located near the edge of the agar tube. As time progresses, the peak in $\varepsilon(r)$ moves inward toward the center of the fiber, and becomes sharp. These features agree with
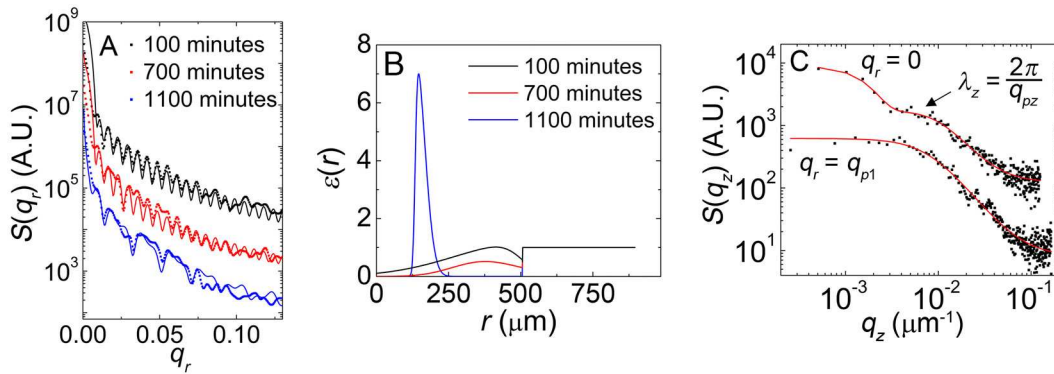
**Fig. 4.** SALS measurements are performed on the collapsing fiber to further explore the cell distribution in time. Along the radial direction, $S(q_r)$ exhibits rapidly oscillating fringes corresponding to the diameter of the agar tube housing the endothelial cell fiber. Over time, a second modulation appears associated with the collapsing fiber (A, dots are experimental data). To estimate the cell distribution, the power spectrum of a minimal model of refractive index variation is fit to the data (A, lines), once again showing a higher cell density near the edge of the fiber than at the center, which sharpens over time (B). Along the meridional direction, a peak occurs at $q_r = 0$ and finite $q_z = q_{pz}$, which does not appear at higher $q_r$ locations (C, $q_r = q_{pl}$ corresponds to $S(q_z)$ centered on the peak of the first fringe along $q_r$. Lines are Lorentzian fits, dots are data). The wavelength associated with the peak at $q_{pz}$, $\lambda_z = 2\pi/q_{pz}$ corresponds to a length scale of about 1 mm.

the progression of cell distribution inferred from absorption measurements, above, and from the qualitative observations of cell density in two-photon fluorescence microscopy.

We observe a broad peak in the SALS measurements along the $q_z$ axis, at $q_r = 0$ and finite $q_z$, indicating a density modulation along the fiber axis. To extract information associated with this peak, we fit the scattering data along the $q_z$ direction with the sum of two Lorentzian peaks: one peak centered at the origin, which reflects a combination of long-wavelength scattering and direct beam, and a second peak centered at a finite $q_z \equiv q_{pz}$. We find that the peak starts at low-$q$ at early times, moving to higher $q$ at later times as the fiber collapses. Throughout the measurement, the spatial length scale associated with this peak, $\lambda_z = 2\pi/q_{pz}$, decreases from about 3 mm to about 1 mm. This length scale is close to the short-wavelength undulations observed in microscopy and macro-photography, described above.

### 2.3 Multi-scale buckling in contracting fibers

The cell fiber undulations observed here are reminiscent of buckling modes that arise from compressive stresses applied along the axis of elastic cylinders. In the classical mathematical descriptions of beam buckling, a compressive static stress is applied to the ends of the model beam, which is balanced along each infinitesimal element along the beam length [20]. When the energy of compression is larger than the energy of bending, the beam buckles with a characteristic shape that depends strongly on boundary conditions at the beam ends and the radial boundary along the beam length, in the case of beams in confinement. There is no externally applied stress applied to the cell fiber measured here. However, the exact same force balance equations can be written down in which internally

generated tensile stresses, balanced across each element, replace the externally applied compressive force. This substitution predicts the same mechanical instabilities as the classical example. Most cell types, including endothelial cells, persistently maintain a state of tensile stress through cytoskeletal contractions, pulling the surrounding ECM inward toward the cell center [1,21].

We consider whether the cell fiber undulations may be mechanical buckling by estimating the forces necessary to generate the characteristic wavelengths determined from our measurements. For classical Euler buckling, the critical buckling stress is $\sigma_{cr} = E(n\pi R/L)^2$, where $E$ is the Young's modulus of the cylinder material, $R$ is the cylinder radius, $L$ is the cylinder length, and $n$ corresponds to wavelength of the buckle. We approximate the cell fiber to have freely pivoting ends, so $L/n = \lambda/2$. We measure the shear modulus of the collagen in oscillatory rheology at 1 Hz up to $\sim 10\%$ strain, finding a shear modulus of $G' = 42$ Pa. Assuming a Poisson's ratio of 1/3, typical of semi-dilute gels, we estimate a Young's modulus of $E \approx 125$ Pa. For the long-wavelength buckling observed with macro-photography, analyzing the case of $\lambda \approx 15$ mm and $R \approx 250\,\mu$m, we find $\sigma_{cr} = 1.4$ Pa.

Single cells generate much more stress than 1.4 Pa, but cells are not close-packed in the fiber; $\sigma_{cr}$ is the average stress per cell required to generate a buckle. For cells at a volume fraction $\phi_c$, each of which generates local stress, $\sigma_c$, we approximate the average stress along the fiber axis as $\langle \sigma_z \rangle = \sigma_c \phi_c/3$, where the 1/3 comes from assuming isotropic stresses. The cell volume fraction is given by $\phi_c = V_c N_c/V_{fiber}$, where $V_c$ is the volume of a typical cell, $N_c$ is the number of cells, and $V_{fiber}$ is the volume of the whole fiber. For a fiber with $R = 250\,\mu$m and $L = 30$ mm, filled with $N_c = 10^5$ cells of volume $V_c = 1500\,\mu$m$^3$, we find $\phi_c = 0.025$; a fiber with this many cells of volume $V_c$ reaches random close packing when $R = 50\,\mu$m, the minimum radius typically reached in a collapsed fiber.
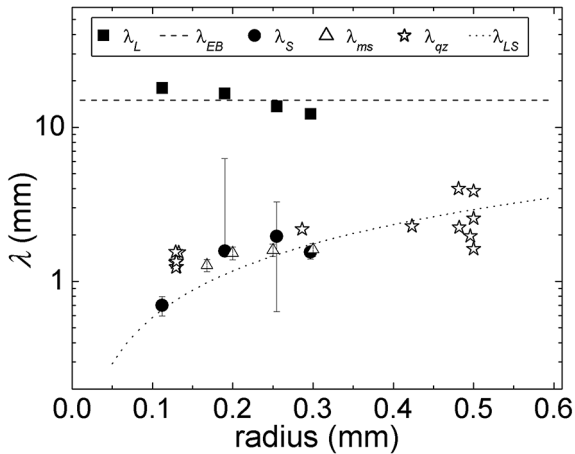
**Fig. 5.** The long-wavelength undulations observed in macro-photography, $\lambda_L$, are of the same order of magnitude as predicted from Euler buckling, though do not scale with radius as predicted (dashed line corresponds to the case where $R = 250$ mm, discussed in the text). The short-wavelength undulations observed in macro-photography ($\lambda_S$), microscopy ($\lambda_{ms}$) and SALS ($\lambda_{qz}$) are of the same order of magnitude predicted by Euler buckling of a beam embedded in a linear elastic medium, and scale with radius as predicted (dashed line is a simultaneous fit to all short-wavelength data).

For buckling to occur $\langle \sigma_z \rangle > \sigma_{cr}$, suggesting the minimum stress each cell must generate is 170 Pa. Most adherent contractile cells, including endothelial cells, generate higher levels of stress than this [22]. Thus, the long-wavelength undulations observed here may be Euler buckling, in which $\lambda_{EB} < L$ arises because the buckling fiber is confined within a rigid agar tube, exciting higher-order bending modes (fig. 5). However, any prediction for $\lambda$ based on Euler buckling would predict $\lambda_{EB}$ increases with radius, yet we measure a decrease in radius. Other factors contributing to this inconsistency in scaling between $\lambda_{EB}$ and $R$ are explored below, in the Discussion section.

Short wavelength buckles can arise in beams embedded in an elastic medium. Mathematically, the effects of the embedding elastic medium are included in the force-balance equations as a term proportional to a shear modulus. The wavelength of the buckle is given by $\lambda = 2\pi(K/G')^{1/4}$, where $G'$ is the shear modulus of the embedding medium, and $K = EI$ is the bending stiffness of the beam; $E$ is the Young's modulus of the beam material and $I$ is the second moment of area [20]. For a uniform beam, $I = \pi R^4/4$, where $R$ is the beam radius. The distribution of cells and collagen throughout the fiber are not known with microscopic detail, so the specific mechanism through which the shear modulus of collagen contributes to the force balance requires further study. Assuming a contribution of collagen shearing over short length scales, we explore the potential role of $G'$ in generating short-wavelength undulations in the cell fiber, with the collagen acting like an elastic reinforcing medium, and leaving $E$ as a fitting parameter. Simultaneously fitting all of the short-wavelength data, measured in macro-photography,

microscopy, and light scattering, we find $E = 53$ Pa. Interestingly, this modulus is about 1/3 the stress required to generate the long-wavelength buckles described above, and is about 1/3 the Young's modulus, also found above. The long-wavelength and short-wavelength analysis could be made self-consistent by using $E = 53$ Pa in the long-wavelength bucking analysis, which would result in a minimum single cell stress required for buckling of about 72 Pa, still well within the range of stress cells can generate. Together, these results suggest that active stress generation or cell bending stiffness, when mismatched with the elasticity of an embedding material like collagen, may drive short-wavelength buckling instabilities.

## 3 Discussion and conclusions

Here we have found that endothelial cells embedded in a thin, cylindrical ECM fiber collectively generate large-scale undulations resembling the sinusoidal morphology typical of blood vessels. The cells appear to congregate more densely at the surface of the fiber than near the fiber center, also crudely mimicking blood vessels. Our analyses of the mechanics underlying these undulations suggest that cytoskeleton-generated contractions drive the collapse and bending of the fiber, and reveal that the undulations may be buckling instabilities. These back-of-the-envelope estimates highlight the need for more thorough theoretical modelling. Here, these models have helped to guide our interpretation of the experimental observations, and serve to motivate the intriguing role played by mechanical instabilities in determining morphology in high-aspect ratio cellular structures. For example, it is possible that local fluctuations in cell density contribute to the short-wavelength undulations observed here, or that tangential forces generated by oriented cell contractions act in a manner analogous to dynein motors that drive microtubule buckling [23,24].

One complication in the analyses performed here is the potential role played by the non-uniform radial distribution of the cells across the fiber. The simplest model of this distribution is a cylindrical shell of finite thickness, rather than a homogeneous beam, which would modify the second area moment, given by $I = \pi(R_o^4 - R_i^4)/4$, where $R_o$ is the outer radius and $R_i$ is the inner radius. Our estimates of the effective shell thickness indicate that the inner radius of the shell is less than 1/2 the outer radius, reducing $I$ by less than a factor of 1/16 (fig. 3I).

Other major concerns are the increase in cell density and collagen concentration during the fiber collapse; the number density of stress-generating cells rises, any stiffness contribution associated with deforming cell assemblies is likely to evolve, and collagen concentration rises. Carefully designed experiments that probe these phenomena are necessary to elucidate this intriguing potential interplay between increased cell concentration and ECM stiffening. It is instructive to observe that with beam buckling in an elastic medium —where our predictions match well with the experiments— the buckling wavelength depends on the ratio of a bending elasticity and a modulus.

If both rise by the same amount, the wavelength does not change. We speculate that one term is associated with cell stiffness and stresses, and the other is associated with the modulus of the ECM. Cell stiffness and stress generation generally rises with increased ECM modulus, so the potential transient effects that occur during fiber collapse may cancel one another out [1]. Future work in which the baseline ECM stiffness is varied while measuring the buckling wavelength will reveal whether this potentially self-correcting effect is built into contraction-generated endothelial cell fiber morphology.

# 4 Materials and methods

## 4.1 Endothelial cell culture

Human aortic endothelial cells (HAECs) are cultured in Endothelial Basal Media (EBM-2) supplemented with vascular endothelial growth factor. The cells are grown to 80–90% confluence, then passaged and centrifuged into a $20\,\mu L$ pellet. This pellet of cells is thoroughly mixed with fresh growth medium and collagen-I monomer (1.5% final concentration), and deposited into the sample chamber. The sample chamber is then incubated at $37\,°C$ and 5% $CO_2$ for 30 minutes before imaging or light scattering measurements to allow for the collagen to gel, and for the cells to spread.

## 4.2 Sample preparation for multi-photon confocal imaging

HAECs are dyed with 5-chloromethylfluorescein diacetate (CMFDA) before centrifuging and being placed within the sample chamber. Samples are incubated for a designated amount of time, then fixed using 3.7% formaldehyde and phosphate buffered saline (PBS) solution. After fixing, the samples are rinsed in PBS buffer and refrigerated.

## 4.3 Small-angle light scattering image processing

The scattering patterns produced by the cell fibers span a dynamic range of approximately $10^5$ counts. To detect intensities over this large dynamic range with a 12-bit digital camera, three images with different exposure times are collected at each time point. The three images are processed with a custom bracketing algorithm written in MATLAB. In each image, saturated pixels are identified and discarded. An additive noise of about 10 counts is subtracted, and any resulting pixels with intensity less than or equal to zero are discarded. The thresholded images are then rescaled by their individual exposure times. The three images are then averaged, accounting for discarded pixels from the thresholding process, producing a seamless bracketed image for each time-point.

## 4.4 Comparison between experimental modalities

Four independent sets of experiments are presented here which produce qualitative and quantitative agreement with one another. All time-lapse measurements including SALS, macro-imaging, and microscopy were performed twice or more, producing consistent results. Two-photon fluorescence microscopy was performed once.

# References

1. D.E. Discher, P. Janmey, Y.-l. Wang, Science **310**, 5751 (2005).
2. A. Harris, P. Wild, D. Stopak, Science **208**, 4440 (1980).
3. M. Dembo, Y.-L. Wang, Biophys. J. **76**, 4 (1999).
4. S. Lehoux, A. Tedgui, J. Biomech. **36**, 5 (2003).
5. B. Langille, R. Brownlee, S. Adamson, Am. J. Physiol. **259**, 28 (1990).
6. R.A. Bomberger *et al.*, J. Surgical Res. **28**, 5 (1980).
7. J.R. Guyton, C.J. Hartley, Am. J. Physiol. **248**, H540 (1985).
8. L. Pellegrino, G. Prencipe, F. Vairo, Minerva Cardioangiol. **46**, 3 (1998).
9. D. Mukherjee, T. Inahara, Am. J. Surgery **149**, 5 (1985).
10. P. Pancera *et al.*, Int. Angiol. **17**, 1 (1998).
11. A.M. Waxman, Microvascular Res. **22**, 1 (1981).
12. R. Beigelman *et al.*, Angiology **61**, 1 (2010).
13. C. Tickle, *Principles of development* (Oxford University Press, 2011).
14. W. Risau, Nature **386**, 6626 (1997).
15. E. Bell, B. Ivarsson, C. Merrill, Proc. Natl. Acad. Sci. U.S.A. **76**, 3 (1979).
16. J. Howard, *Mechanics of motor proteins and the cytoskeleton* (Sinauer Associates Inc., 2001).
17. C.P. Brangwynne *et al.*, Biophys. J. **93**, 1 (2007).
18. C.P. Brangwynne *et al.*, J. Cell Biol. **173**, 5 (2006).
19. L. Cipelletti, D. Weitz, Rev. Sci. Instrum. **70**, 8 (1999).
20. L.D. Landau, E.M. Lifshitz, *Course of Theoretical Physics*, Vol. **7**: *Theory and Elasticity* (Pergamon Press, 1959).
21. D. Vader *et al.*, PLoS ONE **4**, 6 (2009).
22. N. Wang *et al.*, Proc. Natl. Acad. Sci. U.S.A. **98**, 14 (2001).
23. J. Wu *et al.*, Mol. Biol. Cell **22**, 24 (2011).
24. N. Shekhar *et al.*, Cell. Mol. Bioengin. **6**, 2 (2013).